APPLIED PHYSICS

Performing calculus with epsilon-near-zero metamaterials

Hao Li[1]†, Pengyu Fu[1]†, Ziheng Zhou[1], Wangyu Sun[1], Yue Li[1,2]*, Jiamin Wu[2,3]*, Qionghai Dai[2,3]*

Calculus is a fundamental subject in mathematics and extensively used in physics and astronomy. Performing calculus operations by analog computing has received much recent research interest because of its high speed and large data throughput; however, current analog calculus frameworks suffer from bulky sizes and relatively low integration densities. In this work, we introduce the concept of an epsilon-near-zero (ENZ) metamaterial processing unit (MPU) that performs differentiation and integration on analog signals to achieve extreme miniaturization at the subwavelength scale by generating desired dispersions of the ENZ metamaterials with photonic doping. To show the feasibility of this proposal, we further build an experimental analog image edge extraction system with a differentiating ENZ-MPU as its compute core. With a computing density theoretically analyzed to be several tera-operations per second and square micrometer, the proposed ENZ-MPU is scalable and configurable for more complex computations, providing an effective solution for analog calculus operators with extreme computing density and data throughput.

INTRODUCTION

Calculus, usually referred to as differentiation and integration, is a fundamental part of mathematics applied in a variety of fields including geophysics (*1*), astronomy (*2*), biotechnology (*3*), and statistics (*4*), to name a few. Computing the differentiation and integration of a signal is a critical task in various engineering applications exemplified by proportional-integral-derivative (PID) control in automatic control systems (*5*) and images' edge extraction in computer vision (*6*). In the PID controlling, we calculate the time derivatives, integrals, and proportions of the output signal and input them to the system as the feedback to increase the accuracy and stability of system controlling (*7*). Apart from PID controlling, differentiating operation is also exerted to two-dimensional (2D) signals such as images to portray the edge of an input image, which is demanded by image identification applications as either an important functionality or a critical preprocessing approach (*8*). These practical allocations demand the calculus operations to be real-time performed to signals with a compact space and low energy consumption.

Such computing processes are mostly conducted by the digital signal processors (DSPs) of electronic computers in current information technologies; however, physical limitations, including parasitic capacitance, tunneling effects, and cross-talk, prevent electronic DSPs from achieving exponential scaling of their computing density (*9*, *10*) and ultrahigh speed. In recent years, a surge in demand for high-speed computing has motivated numerous researchers to investigate the possibility of performing mathematical operations with photons instead of electrons, i.e., the concept of analog optical computing, to find an alternative path to overcome the speed and efficiency bottlenecks suffered by digital computers (*11*–*13*). Among these studies, some researchers aim at designing all-optical neuromorphic computing platforms by using the deep diffractive neural network (D^2NN) frame (*14*–*18*), the Mach-Zehnder interferometer (MZI) array for chip-scale artificial neural networks (*19*, *20*), and memristors (*21*). Several photonic processors have achieved competitive performance with state-of-the-art electronic devices by harnessing phase-change-material memory arrays (*22*) or fiber dispersion (*23*), demonstrating the superiority of optical computing in speed and efficiency.

Apart from such systematic optical computing works with complex functionalities, to simply perform calculus operations to input signals in an analog manner within a single device has also been investigated by plenty of researches. A traditional architecture for optically performing signal-processing tasks is the 4-*f* system, which is composed of two lensing systems and a filter (*24*). This system is capable of applying linear time-invariant transformations of any form, including all calculus operations, on the impinging electromagnetic field at the expense of a bulky structure and difficulties in chip-scale integration. Metamaterials (*25*), as artificially designed resonant structures for unconventional electromagnetic wave control, are useful for reducing the longitudinal size of photonic computing elements. The concept of computational metamaterials was introduced in (*26*) in the context of applying linear convolutions to spatial optical fields using layered materials much thinner than the traditional 4-*f* system. Metamaterials in 2D form, i.e., metasurfaces, are investigated by researchers to be compatible for analog signal processing within subwavelength thicknesses using methods including space-time modulations (*27*–*29*). Furthermore, they have also been studied to perform spatial differentiation operations (*30*–*33*). The reflection spectrum of a metasurface is also feasible to be controlled, and a temporal differentiator is proposed in (*34*). Moreover, subwavelength metastructures can be used to solve integral equations (*35*). However, although the longitudinal thicknesses are reduced to the subwavelength scale, performing spatial mathematical operations intrinsically yields a large transverse dimension.

Such analog computing devices more easily achieve smaller sizes when they are implemented in time domain by transferring the envelope of input signals to their derivatives when the light is propagating through the device. Fibers are the most preferable transmission waveguides in optics, and consequently, all-fiber differentiators and

[1]Department of Electronic Engineering, Tsinghua University, Beijing 100084, China. [2]Beijing National Research Center for Information Science and Technology, Beijing 100084, China. [3]Department of Automation, Tsinghua University, Beijing 100084, China.
*Corresponding author. Email: lyee@tsinghua.edu.cn (Y.L.); wujiamin@tsinghua.edu.cn (J.W.); daiqionghai@tsinghua.edu.cn (Q.D.)
†These authors contributed equally to this work.

integrators have been first proposed by researchers using coupled fibers (*36*), long-period fiber gratings (*37*, *38*), and fiber Bragg gratings (*39*–*41*). These components are promising for fiber-based all-optical computing systems. Furthermore, to reduce the bulky size of fibers, mathematical operational devices using on-chip silicon waveguides are also proposed (*42*–*44*). In (*42*), a photonic differentiator is designed and experimentally evaluated using a waveguide together with a microring resonator made by silicon. This configuration is also extended to realizing integrators (*43*) and reconfigurable calculus operators (*44*). The utilization of planar light circuit components results in compact geometries and convenience in being packaged into chip scale. However, each processing unit of such an integrated optical computing architecture still has a relatively large size on the order of dozens of wavelengths, facing the same fundamental diffraction limit. This barrier prevents existing optical computing devices from achieving an extremely high computing density, which is defined as the computing speed per area or volume.

To break through this bottleneck, we here propose the concept of an epsilon-near-zero metamaterial processing unit (ENZ-MPU), which is capable of performing calculus operations at the speed of light on the subwavelength scale. Rather than focusing on the spatial modulation of a complex light field with multiple spatial modes for interference, we exploit the spectral modulation of a single-mode light field to process a sequential data stream encoded in the temporal domain. ENZ metamaterials (*45*–*47*) generate a specific dispersion with either a transmission zero or transmission pole instead of ordinary waveguide-based optical circuit elements, thus allowing the size of the structure to be further reduced to the subwavelength level. The dispersion properties of ENZ metamaterials can be tailored by adding either periodic (*48*) or nonperiodic (*49*) nanoparticles, and the latter approach has inspired a new technique with the name of photonic doping (*50*, *51*), which enables control of the permeability of a whole bulky ENZ medium at a single point. To demonstrate the feasibility of our proposal, we manipulated the dispersion properties of an ENZ medium using the technique proposed in (*51*) to perform differentiation and integration. Furthermore, we experimentally verified the method by means of a proof-of-concept image processing system for edge extraction, which was implemented in the microwave frequency band for convenience because of the relatively long wavelengths and correspondingly large fabrication tolerances. Multiple ENZ-MPUs can also be cascaded to perform more complicated operations. With a computing density that is theoretically analyzed to be several tera-operations per second (TOPS) per square micrometer, which is orders of magnitude higher than that of state-of-the-art electronic or photonic processors, the proposed ENZ-MPU provides a promising pathway for next-generation optical integrated circuits with extreme computing density and data throughput.

RESULTS

Theory and configuration of the ENZ-MPU

The general concept of the proposed ENZ-MPU is depicted in Fig. 1. By inserting different dopants into an ENZ host, one can design a different kind of transmission function and perform corresponding mathematical operations on impinging signals in the form of either waveforms or images. Specifically, we demonstrate how to perform differentiation and integration operations as two examples. For differentiation, the ENZ-MPU should have a transmission function of the form $T(\omega) = -i(\omega - \omega_0)$, while for integration, this function should be written as $T(\omega) = i/(\omega - \omega_0)$ (*52*). Here, ω_0 is the angular frequency of the carrier wave. We first focus on how to achieve the transmission function T for differentiation within a waveguide structure. A critical feature of this function is that $T(\omega_0) = 0$ at the carrier wave frequency, where a transmission zero exists. We adopt the metastructures introduced in (*51*), where a photonically doped ENZ medium is studied to achieve total reflection of the impinging wave when the dopant's geometry is suitably engineered. To start with, we consider a 2D waveguide structure as configured in Fig. 2A under a *y*-polarized transverse electromagnetic (TEM) wave's illumination. The device consists of a doped ENZ core with a dielectric block inserted and exhibits a transmission null at ω_0. To improve the differentiation performance, we add an

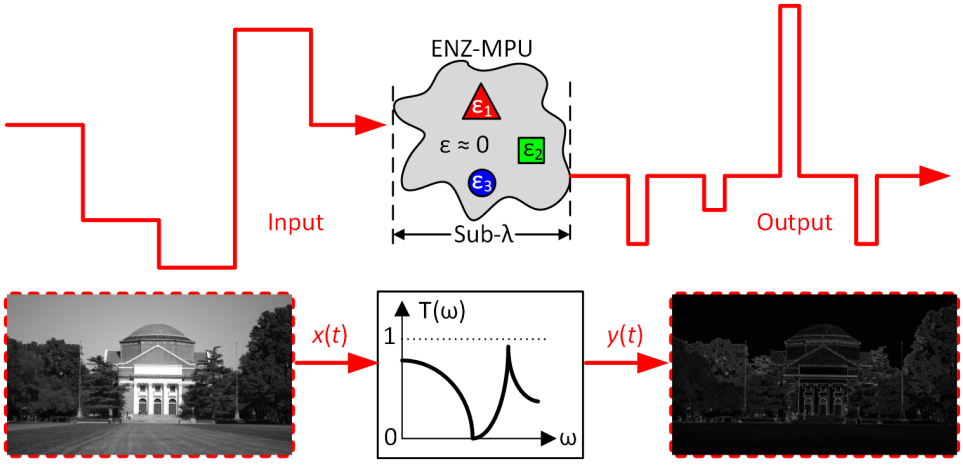

Fig. 1. General concept of the time-domain ENZ-MPU realizing differentiation and integration. A conceptual sketch of tailoring the dispersion and transmittance properties of an ENZ medium using photonic doping techniques to form an ENZ-MPU that applies differentiation operations to input waveforms within an area at the subwavelength scale. By modulating the input waveform to carry images, it is also feasible to apply this concept for image processing by performing differentiation operations on images. Photograph credit: Pengyu Fu, Tsinghua University.

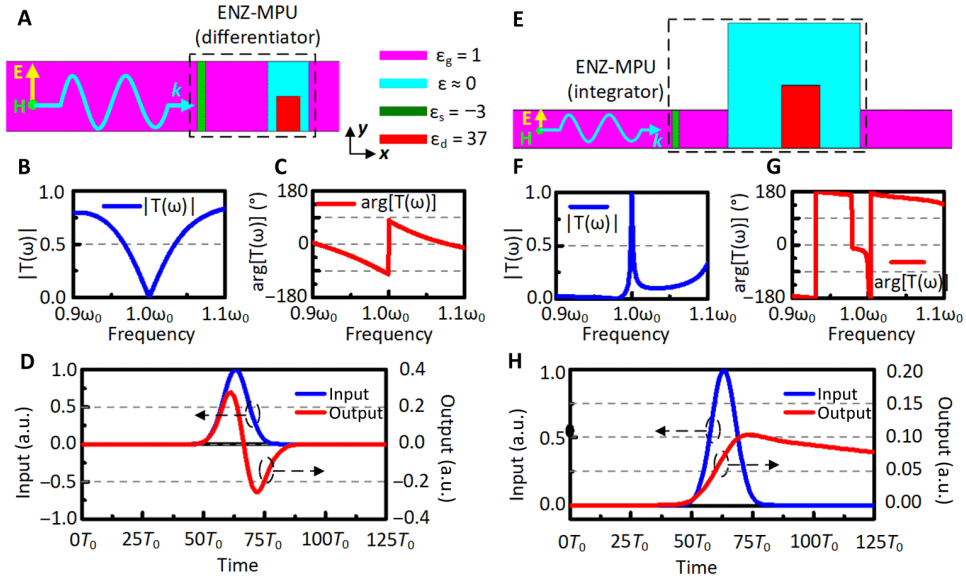

Fig. 2. Results of a time-domain analog differentiator and integrator. (**A**) The configuration of the proposed analog differentiator, (**B** and **C**) the magnitude and phase of the differentiator's transmission function with respect to frequency, (**D**) the temporal response with input consisting of a Gaussian pulse, and (**E** to **H**) the configuration, transmission function, and temporal response of the analog integrator. a.u., arbitrary units.

epsilon-negative (ENG) slab, and a quarter-wavelength waveguide is inserted between the ENG slab and the doped ENZ core. The permittivities at ω_0 of all materials used in the configuration are also provided. The top and bottom walls are assumed to be perfect electric conductors (PECs) for simplicity of analysis, and both the ENZ and ENG materials used here have dispersions described by Drude models, the plasma frequencies of which are ω_0 and $2\omega_0$, respectively. Detailed dimensions are provided in fig. S1. To illustrate the operation mechanism of the proposed device, we start from the dispersion performance of the ENZ material doped with a rectangular dielectric inclusion. According to (*51*), it is reasonable to model this material as a homogeneous ENZ medium with an effective relative permeability of

$$\mu_{r,\mathrm{eff}} = 1 + \sum_{m=1,n=1}^{+\infty} \frac{4 l_d h_d ((-1)^m - 1)^2 ((-1)^n - 1)^2}{A \pi^4 m^2 n^2} \frac{{k_d}^2}{(m\pi/l_d)^2 + (n\pi/2h_d)^2 - {k_d}^2} \quad (1)$$

In this equation, l_d and h_d represent the length and height of the dielectric dopant, respectively. k_d, which is calculated as $k_d = k_0\sqrt{\varepsilon_d}$, denotes the wave number within the dopant, while A is the total cross section of the ENZ medium. We assume that this device operates only near the carrier frequency ω_0 and ignore both material and structural dispersions. In this case, the total transmission function of the whole device is derived to be

$$T(\omega) = i\frac{2Z_0}{2Z_0 - i\omega\mu_{r,\mathrm{eff}}\mu_0 A/h - i\omega {Z_0}^2 \varepsilon_s l_s} \quad (2)$$

Here, Z_0 is the wave impedance within the waveguide and is equal to $\sqrt{\mu_g/\varepsilon_g}$. Detailed mathematical derivations are provided in note S1. From Eq. 1, one can observe that when the condition $(\pi/l_d)^2 + (\pi/2h_d)^2 = {k_d}^2$ is satisfied, the dopant resonates with its TM_{11} mode at ω_0, causing the effective permeability to tend toward infinity. In this case, Eq. 2 can be written in the following form

$$T(\omega) = i\frac{2Z_0}{2Z_0 - i\omega\mu_1 A/h - i\omega {Z_0}^2 \varepsilon_s l_s - 16i\omega^3\mu_0 l_d h_d/\pi^4 h(\omega^2 - \omega_0^2)} \quad (3)$$

where μ_1 is equal to

$$\mu_1 = \mu_0 \sum_{m=1,n=1,\mathrm{mn}>1}^{+\infty} \frac{4 l_d h_d ((-1)^m - 1)^2 ((-1)^n - 1)^2}{A \pi^4 m^2 n^2} \frac{\varepsilon_d {\omega_0}^2}{c^2[(m\pi/l_d)^2 + (n\pi/2h_d)^2] - \varepsilon_d {\omega_0}^2} \quad (4)$$

which is a finite value near ω_0. When the condition ${Z_0}^2\varepsilon_s l_s = \mu_0 A$ is satisfied, within a narrow frequency range near ω_0, $T(\omega)$ is approximately a linear function of the frequency difference $(\omega - \omega_0)$ because it is equal to

$$T(\omega) = -\frac{\pi^4 Z_0 h}{2\mu_0 l_d h_d {\omega_0}^2}(\omega - \omega_0) + o(\omega - \omega_0)^2 \quad (5)$$

Thus, we can create a linear response function with a zero spot in the spectral domain, which can be viewed as an ideal differentiator with the zero spot located at the center frequency of the carrier wave. Furthermore, by introducing an ENG slab that acts as a shunt lumped inductor (*53*), the linearity is enhanced compared with using a doped ENZ medium only. When the condition ${Z_0}^2\varepsilon_s l_s = \mu_0 A$ is satisfied, both the linearity and the differentiating bandwidth reach their optima. A detailed parametric study is presented in note S2 and figs. S2 and S3, in which it is demonstrated that by choosing $\varepsilon_s = -3$, we can obtain a symmetric and highly linear $T(\omega)$ near ω_0. In this way, the ENZ-MPU is devised as a first-order differentiator.

To validate the analytical derivation above, we performed a numerical simulation using CST Microwave Studio 2016. The magnitude and phase of the transmission function of the differentiator depicted in Fig. 2A are shown in Fig. 2 (B and C, respectively), from which one can observe that the magnitude of $T(\omega)$ is proportional

to the absolute difference between the frequency and the carrier frequency, $|\omega - \omega_0|$, within a frequency range from approximately $0.95\omega_0$ to $1.05\omega_0$. The phase of the differentiator is shown in Fig. 2C. A phase inverse of 180° is observed exactly at ω_0 and consistent with the ideal differentiating response. In addition, the transmission phase varies linearly over frequency, and this effect introduces only the time delay without any distortions to the output differentiated signal, as depicted in Fig. 2D. These results in the frequency domain reveal that the ENZ differentiator is capable of calculating the first-order derivative of an input signal as long as its bandwidth is smaller than $0.1\omega_0$, setting a bound on the computing speed. To further verify the device's performance, we applied an impinging Gaussian impulse to it, and both the input and output signal envelopes are depicted in Fig. 2D. The input Gaussian impulse is characterized by

$$x(t) = \sin(\omega_0 t)\, e^{-\frac{(t-62.5T_0)^2}{50T_0^2}} \tag{6}$$

where $T_0 = \pi/\omega_0$. In this case, the device's operating bandwidth is wide enough to differentiate this signal. As seen in Fig. 2D, the output signal is indeed the derivative of $x(t)$, thus providing a verification of the proposed design. Moreover, this first-order differentiator can be easily extended to higher-order differentiators by cascading several identical devices. To build such an n-order differentiator, n first-order differentiators and $(n - 1)$ nonreciprocal or lossy interconnect components are required. Detailed results and analysis for the case of $n = 2$ are presented in fig. S4 with high precision.

In addition to such a differentiating system, similar structures can be used for other operations, such as finite-time integration, with only parametric changes. In Fig. 2E, we show another example of an ENZ-MPU with the function of integration based on similar doped ENZ metastructures obtained by adjusting only two parameters during the doping process, namely, the ENZ medium's cross section A and the resonant frequency of the dopant. Enlarging A leads to an enhanced quality factor and a transmission pole at ω_0, i.e., the transmittance has a nonzero value only within an ultranarrow frequency range around ω_0, where $\mu_{\text{eff}} \approx 0$. Simulations of this device were also performed, and the simulated transmission function results are shown in Fig. 2 (F and G), where both the magnitude and phase distributions resemble the ideal response well. The temporal response was also tested using the same Gaussian impulse used for the differentiator. As shown in Fig. 2H, the integrator is able to generate an output of $y(t) = \int x(t)\mathrm{d}t$, despite the existence of a slight decay.

Implementation of the ENZ-MPU

In the above analysis, we have fully investigated the basic principle of performing temporal differentiations and integrations using lossless metastructures with artificially defined permittivities. To further validate the engineering potential of the proposed design, we also tested the performance when using naturally occurring materials instead of ideal ones with arbitrary ε_r. As illustrated in Fig. 2, materials with both near-zero and negative permittivities can be used to construct the device. However, naturally existing ENG and ENZ materials, i.e., plasmonic materials, suffer from severe losses when operating near or below the plasma frequency (*54*). To address this problem, we make use of rectangular waveguides to emulate ENZ and ENG materials because this method has been validated in (*55*), which proposed a hollow rectangular waveguide coated with silver and demonstrated the equivalence between this structure and ENZ metamaterials at mid-infrared (IR) frequencies. Similar to the configuration in (*55*), we use waveguides filled with air, SiO_2, and Si to emulate ENG, ENZ, and epsilon-positive (EPS) materials and construct a differentiator based on these equivalent metamaterials. It should be noted that because of the limitations of the available materials in this frequency range, adding a single ENG slab on one side of the doped ENZ core is not sufficient to achieve the optimal differentiating performance. Therefore, we slightly modify the structure by duplicating the ENG slab and quarter-wavelength waveguide on the other side of the ENZ core. In addition, the dopant within the ENZ medium is elevated from the silver ground to decrease the loss of the device. It is necessary to mention that because the dopant is elevated from the silver boundary, the permeability is calculated in a different manner as

$$\mu_{\text{r,eff}} = 1 + \sum_{m=1,n=1}^{+\infty} \frac{2\, l_{\text{d}} h_{\text{d}} ((-1)^m - 1)^2 ((-1)^n - 1)^2}{A \pi^4 m^2 n^2} \frac{{k_{\text{d}}}^2}{(m\pi/l_{\text{d}})^2 + (n\pi/h_{\text{d}})^2 - {k_{\text{d}}}^2} \tag{7}$$

The detailed configuration and dimensions together with the simulated results are provided in fig. S5, which shows that this design shares similar performance to the ideal one. The footprint of this differentiator devised to operate in the mid-IR band is 1 μm by 1.05 μm, which is equal to $0.35 \times 0.37\ {\lambda_0}^2$, where λ_0 is the free-space wavelength (2.83 μm here) at the carrier frequency.

Here, we theoretically examine the computing speed of the proposed device by comparing it to a DSP, which is able to perform the same mathematical operations on equivalent input digital sequences. A digital differentiator performs f_s mathematical operations per second when calculating the derivative of a discrete signal with a sampling rate of f_s because it calculates $y(n) = x(n + 1) - x(n)$ for each sample. According to the Nyquist theorem, such an input digital signal contains the full information of a baseband analog signal with a bandwidth of $\Delta f = f_s/2$. For our proposed device, an operation bandwidth of $2\Delta f$ is required to process such an analog input, which is modulated to have a spectrum ranging from $(f_0 - \Delta f)$ to $(f_0 + \Delta f)$. Consequently, the maximum computing speed of the proposed differentiator is quantitatively expressed as $f_{s,\,\max} = \mathrm{BW}_{\max}$ operations per second, which represents the maximum operating bandwidth. As shown in fig. S5, we numerically tested the bandwidth by observing the error rate for a Gaussian impulse input with a spectrum of $X(F) = \exp[-(f - f_0)^2/2\sigma_f^2]$, where the bandwidth is defined as $2\sigma_f$ (see Materials and Methods). For an error rate lower than 5%, this device exhibits a differentiating bandwidth of 12.0 THz when the carrier frequency is 106 THz, corresponding to a computing speed of 12.0 TOPS. Furthermore, the computing density was also calculated by dividing the computing speed by the footprint, yielding a result of 11,400,000 TOPS/mm^2 according to the simulations. In Table 1, a theoretical comparison is presented between our work and other state-of-the-art methods to perform differentiation operations. The D^2NN (*17*) is designed for handling general tasks and is also feasible to differentiate an input signal. Optical differentiators (*36*, *42*, *44*) are specifically designed for calculating the derivatives of the input light, and the computing speeds of these differentiators are characterized by their bandwidths. The differentiator proposed in (*34*) operates in microwave frequencies based on programmable metasurfaces, while the computing density in its recent form is relatively low. The DSPs (*56*, *57*) are also listed in the table as references.

Table 1. Comparison of theoretical computing performance among various methods of differentiation. TPU, tensor processing unit, GPU, graphic processing unit.

Reference	Methods	Footprint (mm^2)	Computing speed (TOPS)	Computing density (TOPS/mm^2)
(*17*)	D^2NN	26.54	240.1	9.04
(*34*)	Metasurface	1.56×10^6	0.015	9.62×10^{-9}
(*36*)	Coupled fiber	0.036	25.0	694
(*42*)	Silicon microring resonator	0.00502	0.01	1.99
(*44*)	MZI array	3.0	0.055	18.3
(*56*)	Google TPU	331	92	0.28
(*57*)	Nvidia GPU	470	47	0.10
Proposed	**Doped-ENZ**	$\mathbf{1.05 \times 10^{-6}}$	**12.0**	**11,400,000**

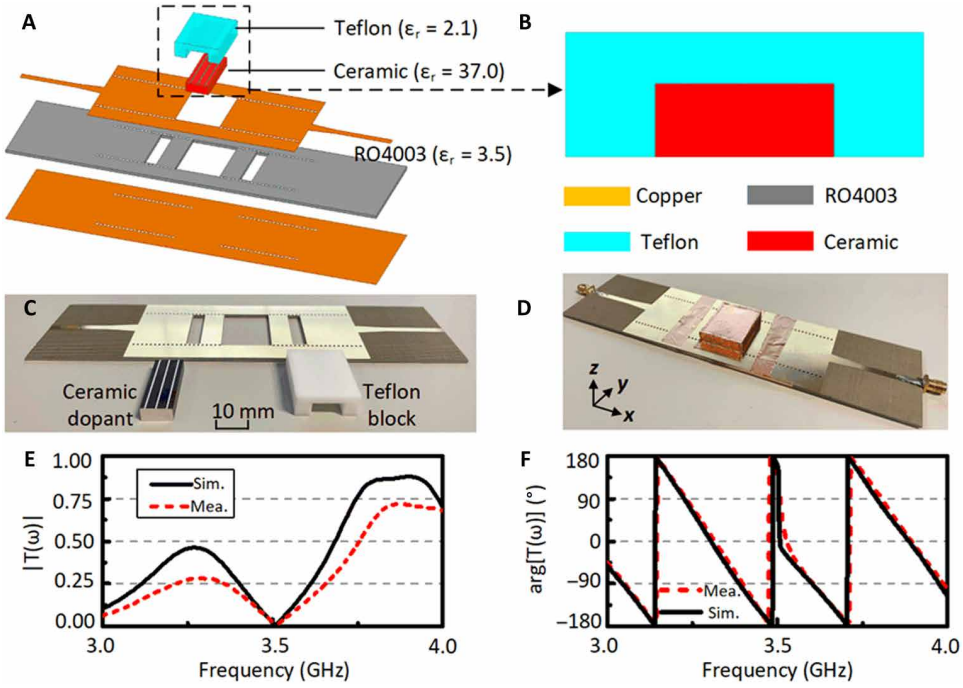

Fig. 3. Fabricated prototype and the measured results of the proposed differentiator in the microwave band. (**A**) Exploded view of the configuration of the differentiator. (**B**) Zoomed-in view of the U-shaped Teflon and the ceramic dopant. (**C**) Photograph of the fabricated PCB, ceramic dopant, and U-shaped Teflon block placed separately. (**D**) Photograph of the assembled prototype. (**E** and **F**) Simulated and measured transmittance magnitudes and phases as functions of frequency.

Although the proposed differentiator cannot handle tasks as complex as the D^2NN (*17*) and DSPs (*56*, *57*) do, it can achieve a high computing speed in a specific task of differentiation within a subwavelength scale, demonstrating an unprecedented computing density corresponding to an improvement of multiple orders of magnitude than previously reported designs.

In addition to the mid-IR frequency differentiator discussed above, this concept is also valid for microwave frequencies, for which both fabrication and measurement are more convenient than for optical frequencies. Similar to the optical case, we choose to devise a differentiator based on a substrate-integrated waveguide structure (*58*) and waveguides emulating metamaterials. Specifically, the configuration of the microwave differentiator is depicted in Fig. 3, where RO4003, Teflon, and air serve as equivalent EPS, ENZ, and ENG materials with relative permittivities of $\varepsilon_r = 1.4$, $\varepsilon_r = 0$, and $\varepsilon_r = -2.1$. The detailed dimensions are provided in fig. S6. For experimental validation, we fabricated a prototype of the differentiating MPU by first fabricating the U-shaped Teflon brick, ceramic block, and printed circuit board (PCB) separately and then assembling them together. Photographs of the three individual components and the assembled device are shown in Fig. 3 (C and D, respectively). The detailed geometries, fabrication methods, and photographs of the fabricated prototype are shown in fig. S6 and the "Fabrication methods" section in Materials and Methods. After the assembly process, we measured the transmittance of the device using a vector network analyzer, and both the simulated and measured results are plotted in Fig. 3 (E and F). In general, the measured and simulated results match well with each other and exhibit high linearity near $f_0 = 3.5$ GHz, demonstrating a good-quality differentiation response. The differentiating bandwidth is 250 MHz (3375 to 3625 MHz) where the S_{21} is a linear function of frequency, and this result is much wider than that of the microwave differentiator reported in

(*34*) but within a much smaller dimension. Some nonideal factors, including fabrication errors, lead to a higher $T(\omega_0)$ at the center frequency of the differentiator, which is measured to be nearly −30 dB, larger than the simulated value. In the following section, we will demonstrate that the transmission null must be improved when constructing a whole computing system. Moreover, different ENZ-MPUs can be cascaded to fit higher-order complex responses in the frequency domain. To verify this concept, we further tested a second-order differentiator constructed by cascading two first-order differentiators with an isolator, as shown in fig. S7; the measured experimental response is shown in fig. S8. All these results reveal that our ENZ-MPU architecture can perform high-speed differential and integral operations with extremely small footprints.

ENZ-MPU image processing system and experimental validation

To experimentally validate the ENZ-based analog computing architecture, we built a proof-of-concept integrated data processing platform using a differentiator as the computing core. In this system, the signal flows along the black arrows, as depicted in Fig. 4A; it first impinges on the system in a digital form, then is converted into an analog signal by being modulated onto a carrier wave using amplitude modulation (AM), is subsequently processed by the differentiator, and is lastly demodulated to obtain a digital output. As mentioned above, because of fabrication error and leakage, the transmittance at f_0 = 3.5 GHz is not exactly zero as simulated but might have a small finite value. To address this problem, we design a bypass filter using an attenuator and phase shifter to achieve attenuation with the same magnitude as $T(\omega_0)$ but the inverse phase, which can eliminate the small direct transmission of the input signal at ω_0. The input analog signal is divided into these two branches by a power divider (PD), and the total output is formed by combining the outputs of the two branches using a PD. The assembled system is shown in Fig. 4B; in this system, modulation and demodulation are realized by means of a universal software radio peripheral (USRP) device.

To examine the data processing capabilities of this system, we tested whether it is able to extract the edges in input images. Edge extraction is a common procedure for extracting object features in machine vision, image processing, and computer vision (*6*). However, with the exponential increase in the number of sensor pixels necessary for high-resolution wide-field imaging, even such a simple operation requires extensive computing resources in practical applications (*59*). Here, we demonstrate that our proposed differentiator and data processing system are able to handle this task. Because the differentiation operation is performed in the temporal domain, only data sequences are appropriate inputs. The general concept of

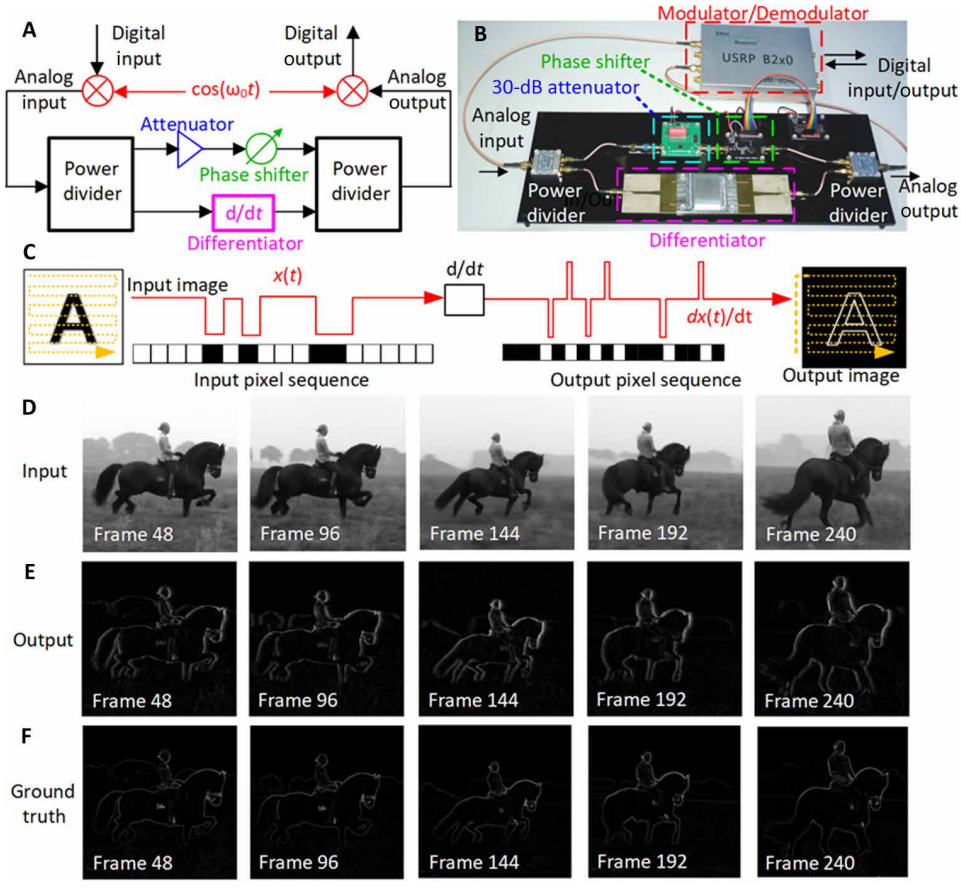

Fig. 4. Experimental validation of the proposed ENZ-MPU at microwave frequencies. (**A**) Schematic architecture of the RF module of the image processing system, (**B**) photograph of the whole image processing system with an ENZ differentiator as the compute core, (**C**) a schematic graph of the image processing platform, (**D**) snapshots of five images taken from a 240-frame video provided as input to the system, (**E**) experimental output images corresponding to the images in (D), and (**F**) ground-truth derivatives for the images in (D). The original video is available in (*60*).

the image processing platform is illustrated in Fig. 4C. We first transform an image into a data stream by cascading each line of the image into an input sequence. After this, the input sequence is modulated onto the carrier wave ω_0 and transmitted to the differentiator. Last, the output signal is demodulated, and an output image is generated by reorganizing the output sequence into a 2D matrix. This process can be applied to both analog inputs and digital ones. For analog inputs, we present a possible schematic for connecting the imaging system to this differentiating unit in fig. S9. For simple implementations with digital inputs, the inputs are first converted into bit streams and then modulated into analog signals, which can be processed by the proposed device. We performed numerical simulations of the whole processing pipeline. Here, we chose various digital images and investigated the output responses based on the architecture proposed above. For the three input images depicted in fig. S10 (A to C), the simulated outputs are shown in fig. S10 (D to F) and are seen to agree well with the ground truth.

Then, we further performed experimental verifications based on the device and system discussed above by experimentally testing the entire system for the function of edge detection in streaming media. Although the analog computing module is capable of handling real-time data, both digital processing on a PC and digital-to-analog conversion are time consuming. The detailed time delays of the PC and USRP are provided in Materials and Methods. In Fig. 4D, we present five frames of a video (*60*) as specific examples, together with their corresponding experimental outputs in Fig. 4E. By comparison with the ground truth shown in Fig. 4F, one can see that the output images effectively capture the profiles of the input images despite some loss in resolution.

DISCUSSION

Here, we analytically, numerically, and experimentally demonstrate performing calculus operations at the speed of light within subwavelength-scale ENZ metamaterials. By tailoring the ENZ-based dispersion, either differentiation or integration can be performed in the temporal domain when a single-mode light field passes through the ENZ metamaterials. The MPU is first analytically investigated in theory to predict its performance and then numerically validated using both ideal and naturally occurring materials. Last, it is experimentally verified in the microwave band, exhibiting a theoretical maximum computing density of up to 11.4 TOPS/μm^2. In addition, the proposed ENZ differentiator is scalable to configurations implementing higher-order complex computations. We have developed an image processing system using the ENZ differentiator as the compute core to experimentally demonstrate its performance in edge detection. By enabling optical computing at the subwavelength scale, the proposed ENZ-MPU offers a promising solution for next-generation optical integrated circuits with the merits of ultra-miniaturization and dense integration.

MATERIALS AND METHODS

Numerical full-wave simulations

The numerical simulations on the 3D structure have been carried out with the frequency domain solver of CST Microwave Studio 2016. For ideal configurations, we assign PEC boundaries on the y_{min} and y_{max} planes while assigning perfect magnetic conductor (PMC) boundaries on the z_{min} and z_{max} planes, thus allowing the propagation of TEM waves within the waveguide. For excitation, we use wave ports at the end of the input and output waveguides. For simulations on both the mid-IR differentiator and the fabricated microwave differentiator, we use open boundary instead of PEC and PMC. The materials' optical properties in mid-IR are according to the standard material library of CST Microwave Studio.

Simulation of time-domain data processing

The simulated results of waveforms are numerically calculated by MATLAB R2016a. We numerically perform a discrete Fourier transformation (DFT) to the input signal, then multiply it with the simulated transmission function to generate an output spectrum, and lastly calculate the output waveform by performing inverse DFT. The simulations on image edge detection are also completed by MATLAB R2016a where we set the data rate of input signal to be 400 Mbps.

Error analysis

To describe the error performance of the proposed differentiator, we mainly use simulations by MATLAB R2016a. To be specific, we impinge a Gaussian impulse with different variations to represent the input signal with different bandwidths. The error rate is calculated by $\mathrm{ERR} = \int[y(t) - y_0(t)]^2 dt / \int y_0^2(t) dt$, where $y(t)$ is the output signal and $y_0(t)$ is the ground truth. In terms of bandwidth, we consider that the bandwidth of Gaussian impulse input with a spectrum of $X(f) = \exp[-(f - f_0)^2/2\sigma_f^2]$ is $2\sigma_f$ because more than 95% of the total power lies in the frequency range $[f_0 - 2\sigma_f, f_0 + 2\sigma_f]$.

Fabrication methods

The prototype is fabricated using standard PCB technology. A U-shaped Teflon block is fabricated, inside which a dielectric block composed by JJD37-6 microwave ceramic with a relative permittivity of 37.0 and a loss tangent of 0.001 is assembled. Three metal wires are printed on the top of the ceramic block for suppressing degenerated resonant modes. Two subminiaturized A coaxial connectors are soldered to the input and output microstrip lines. When assembling the prototype, we first insert the ceramic block into the U-shaped Teflon to form "doped" Teflon, then insert this doped Teflon to the rectangular hole in the PCB, and lastly coated them with copper foils. The ENG slabs are made by covering the hollow region in RO4003 substrate with copper foils. To further prevent the leakage from fabrication tolerances, we screwed an aluminum cover for shielding.

Operating mechanism of the USRP

The radio frequency (RF) system is constructed by PDs, tunable phase shifters and attenuators, and the fabricated prototype. The whole edge detection system contains the RF system mentioned above and a USRP, which offers AM of input digital signals and demodulation for output RF signals with a maximum data rate of 125 kbps. The detailed modulation process is launched by first converting the input bit stream to a baseband analog signal and then mixing this signal with the RF carrier wave, and the reverse process is for the demodulating.

Time delay analysis of the experimental system

The input and output digital signals are processed by a PC, on which runs a MATLAB program encoding and decoding the data stream. Using the timing program in MATLAB, the time delays of

the MATLAB encoding and decoding program and USRP are measured to be 663.3 and 146.1 ms on average, respectively, which are much longer than that of the device itself.

Power consumption

In this experiment, the USRP device is powered by a DC voltage of 5 V and a DC current of 1 A through a universal serial bus so that the total power consumption of the whole system is 5 W. The major part of the input power is used for signal processing and communication with the PC, while a small amount is converted into RF power. In particular, the power of the RF signal generated by USRP and impinged to the MPU is 10 mW. Consequently, we consider the power consumption of the MPU to be 10 mW in our experimental setup.

SUPPLEMENTARY MATERIALS

Supplementary material for this article is available at https://science.org/doi/10.1126/sciadv.abq6198

REFERENCES AND NOTES

1. M. Tong, G. Q. Wang, G. C. Lee, Time derivative of earthquake acceleration. *Earthq. Engin. Engin. Vib.* **4**, 1–16 (2005).
2. A. Pasqua, S. Chattopadhyay, On the dynamics of dark energy with higher time derivatives of hubble parameter in El-Nabulsi fractional action cosmology. *Int. J. Theor. Phys.* **53**, 435–448 (2014).
3. M. H. Zwietering, I. Jongenburger, F. M. Rombouts, K. Van't Riet, Modeling of the bacterial growth curve. *Environ. Microbiol.* **56**, 1875–1881 (1990).
4. T. Górecki, M. Łuczak, First and second derivatives in time series classification using DTW. *Commun. Stat. Simul. Comput.* **43**, 2081–2092 (2014).
5. K. H. Ang, G. Chong, Y. Li, PID control system analysis, design, and technology. *IEEE Trans. Control Syst. Technol.* **13**, 559–576 (2005).
6. V. Torre, T. A. Poggio, On edge detection. *IEEE Trans. Pattern Anal. Mach. Intell.* **PAMI-8**, 147–163 (1986).
7. J. G. Ziegler, N. B. Nichols, Optimum settings for automatic controllers. *Trans. ASME* **64**, 759–768 (1942).
8. D. Selvakarthi, D. Sivabalaselvamani, S. Ashwath, A. P. A. Kalaivanan, K. Manikandan, C. Pradeep, Edge detection and object identification for vision enhancement at rescue operations using deep learning techniques, in *2022 International Conference on Computer Communication and Informatics (ICCCI)* (Coimbatore, India, 25 to 27 January 2022).
9. H. J. Caulfield, S. Dolev, Why future supercomputing requires optics. *Nat. Photonics* **4**, 261–263 (2010).
10. M. M. Waldrop, The chips are down for Moore's law. *Nature* **530**, 144–147 (2016).
11. K. Preston, *Coherent Optical Computers* (McGraw-Hill, 1972).
12. D. Solli, B. Jalali, Analog optical computing. *Nat. Photonics* **9**, 704–706 (2015).
13. R. Athale, D. Psaltis, Optical computing: Past and future. *Opt. Photonics News* **27**, 32–39 (2016).
14. X. Lin, Y. Rivenson, N. T. Yardimci, M. Veli, Y. Luo, M. Jarrahiand, A. Ozcan, All-optical machine learning using diffractive deep neural networks. *Science* **361**, 1004–1008 (2018).
15. T. Yan, J. Wu, T. Zhou, H. Xie, F. Xu, J. Fan, L. Fang, X. Lin, Q. Dai, Fourier-space diffractive deep neural network. *Phys. Rev. Lett.* **123**, 023901 (2019).
16. T. Zhou, L. Fang, T. Yan, J. Wu, Y. Li, J. Fan, H. Wu, X. Lin, Q. Dai, In situ optical backpropagation training of diffractive optical neural networks. *Photonics Res.* **8**, 940–953 (2020).
17. T. Zhou, X. Lin, J. Wu, Y. Chen, H. Xie, Y. Li, J. Fan, H. Wu, L. Fang, Q. Dai, Large-scale neuromorphic optoelectronic computing with a reconfigurable diffractive processing unit. *Nat. Photonics* **15**, 367–373 (2021).
18. C. Liu, Q. Ma, Z. J. Luo, Q. R. Hong, Q. Xiao, H. C. Zhang, L. Miao, W. M. Yu, Q. Cheng, L. Li, T. J. Cui, A programmable diffractive deep neural network based on a digital-coding metasurface array. *Nat. Electron.* **5**, 113–122 (2022).
19. Y. Shen, N. Harris, S. Skirlo, M. Prabhu, T. Baehr-Jones, M. Hochberg, X. Sun, S. Zhao, H. Larochelle, D. Englund, M. Soljačić, Deep learning with coherent nanophotonic circuits. *Nat. Photonics* **11**, 441–446 (2017).
20. I. A. D. Williamson, T. W. Hughes, M. Minkov, B. Bartlett, S. Pai, S. Fan, Reprogrammable electro-optic nonlinear activation functions for optical neural networks. *IEEE J. Sel. Top. Quantum Electron.* **26**, 1–12 (2020).
21. A. Emboras, I. Goykhman, B. Desiatov, N. Mazurski, L. Stern, J. Shappir, U. Levy, Nanoscale plasmonic memristor with optical readout functionality. *Nano Lett.* **13**, 6151–6155 (2013).
22. J. Feldmann, N. Youngblood, M. Karpov, H. Gehring, X. Li, M. Stappers, M. Le Gallo, X. Fu, A. Lukashchuk, A. S. Raja, J. Liu, C. D. Wright, A. Sebastian, T. J. Kippenberg, W. H. P. Pernice, H. Bhaskaran, Parallel convolutional processing using an integrated photonic tensor core. *Nature* **589**, 52–58 (2021).
23. X. Xu, M. Tan, B. Corcoran, J. Wu, A. Boes, T. G. Nguyen, S. T. Chu, B. E. Little, D. G. Hicks, R. Morandotti, A. Mitchell, D. J. Moss, 11 TOPS photonic convolutional accelerator for optical neural networks. *Nature* **589**, 44–51 (2021).
24. J. Goodman, *Introduction to Fourier Optics* (McGraw-Hill, ed. 2, 1996).
25. N. Liu, H. Guo, L. Fu, S. Kaiser, H. Schweizer, H. Giessen, Three-dimensional photonic metamaterials at optical frequencies. *Nat. Mater.* **7**, 31–37 (2008).
26. A. Silva, F. Monticone, G. Castaldi, V. Galdi, A. Alù, N. Engheta, Performing mathematical operations with metamaterials. *Science* **343**, 160–163 (2014).
27. H. Rajabalipanah, A. Abdolali, S. Iqbal, L. Zhang, T. J. Cui, Analog signal processing through space-time digital metasurfaces. *Nanophotonics* **10**, 1753–1764 (2021).
28. T. Cui, M. Qi, X. Wan, J. Zhao, Q. Cheng, Coding metamaterials, digital metamaterials and programmable metamaterials. *Light Sci. Appl.* **3**, e218 (2014).
29. L. Zhang, X. Q. Chen, S. Liu, Q. Zhang, J. Zhao, J. Y. Dai, G. D. Bai, X. Wan, Q. Cheng, G. Castaldi, V. Galdi, T. J. Cui, Space-time-coding digital metasurfaces. *Nat. Commun.* **9**, 4334 (2018).
30. T. Zhu, Y. Zhou, Y. Lou, H. Ye, M. Qiu, Z. Ruan, S. Fan, Plasmonic computing of spatial differentiation. *Nat. Commun.* **8**, 15391 (2017).
31. S. A. Ramezani, K. Arik, A. Khavasi, Z. Kavehvash, Analog computing using graphene-based metalines. *Opt. Lett.* **40**, 5239–5242 (2015).
32. T. Zhu, C. Guo, J. Huang, H. Wang, M. Orenstein, Z. Ruan, S. Fan, Topological optical differentiator. *Nat. Commun.* **12**, 680 (2021).
33. W. Zhang, X. Zhang, Backscattering-immune computing of spatial differentiation by nonreciprocal plasmonics. *Phys. Rev. Appl.* **11**, 054033 (2019).
34. J. Sol, D. R. Smith, P. del Hougne, Meta-programmable analog differentiator. *Nat. Commun.* **13**, 1713 (2022).
35. M. Estakhri, B. Edwards, N. Engheta, Inverse-designed metastructures that solve equations. *Science* **363**, 1333–1338 (2019).
36. M. Li, H. S. Jeong, J. Azaña, T. J. Ahn, 25-terahertz-bandwidth all-optical temporal differentiator. *Opt. Express* **20**, 28273–28280 (2012).
37. D. Krčmařík, R. Slavík, Y. Park, M. Kulishov, J. Azaña, First-order loss-less differentiators using long period gratings made in Er-doped fibers. *Opt. Express* **17**, 461–471 (2009).
38. M. Kulishov, D. Krčmařík, R. Slavík, Design of terahertz-bandwidth arbitrary-order temporal differentiators based on long-period fiber gratings. *Opt. Lett.* **32**, 2978–2980 (2007).
39. M. Li, D. Janner, J. P. Yao, V. Pruneri, Arbitrary-order all-fiber temporal differentiator based on a fiber Bragg grating: Design and experimental demonstration. *Opt. Express* **17**, 19798–19807 (2009).
40. M. A. Preciado, M. A. Muriel, Design of an ultrafast all-optical differentiator based on a fiber Bragg grating in transmission. *Opt. Lett.* **33**, 2458–2460 (2008).
41. L.-M. Rivas, K. Singh, A. Carballar, J. Azaña, Arbitrary-order ultra-broadband all-optical differentiators based on fiber Bragg gratings. *IEEE Photonics Technol. Lett.* **19**, 1209–1211 (2007).
42. F. Liu, T. Wang, L. Qiang, T. Ye, Z. Zhang, M. Qiu, Y. Su, Compact optical temporal differentiator based on silicon microring resonator. *Opt. Express* **16**, 15880–15886 (2008).
43. M. Ferrera, Y. Park, L. Razzari, B. E. Little, S. T. Chu, R. Morandotti, D. J. Moss, J. Azaña, On-chip CMOS-compatible all-optical integrator. *Nat. Commun.* **1**, 29 (2010).
44. W. Liu, M. Li, R. Guzzon, E. J. Norberg, J. S. Parker, M. Lu, L. A. Coldren, J. Yao, A fully reconfigurable photonic integrated signal processor. *Nat. Photonics* **10**, 190–195 (2016).
45. I. Liberal, N. Engheta, Near-zero refractive index photonics. *Nat. Photonics* **11**, 149–158 (2017).
46. B. Edwards, A. Alù, M. E. Young, M. Silveirinha, N. Engheta, Experimental verification of epsilon-near-zero metamaterial coupling and energy squeezing using a microwave waveguide. *Phys. Rev. Lett.* **100**, 033903 (2008).
47. Y. Li, S. Kita, P. Muñozet, O. Reshef, D. I. Vulis, M. Yin, M. Lončar, E. Mazur, On-chip zero-index metamaterials. *Nat. Photonics* **9**, 738–742 (2015).
48. Y. He, Y. Li, Z. Zhou, H. Li, Y. Hou, S. Liao, P.-Y. Chen, Wideband epsilon-near-zero supercoupling control through substrate-integrated impedance surface. *Adv. Theory Simul.* **2**, 1900059 (2019).
49. V. C. Nguyen, L. Chen, K. Halterman, Total transmission and total reflection by zero index metamaterials with defects. *Phys. Rev. Lett.* **105**, 233908 (2010).
50. I. Liberal, A. M. Mahmoud, Y. Li, B. Edwards, N. Engheta, Photonic doping of epsilon-near-zero media. *Science* **355**, 1058–1062 (2017).
51. Z. Zhou, Y. Li, H. Li, I. Liberal, N. Engheta, Substrate-integrated photonic doping for near-zero-index devices. *Nat. Commun.* **10**, 4132 (2019).
52. L. Venema, Photonics technologies. *Nat. Insight* **424**, 809 (2003).
53. Y. Li, I. Liberal, C. Della Giovampaola, N. Engheta, Waveguide metatronics: Lumped circuitry based on structural dispersion. *Sci. Adv.* **2**, e1501790 (2016).
54. N. Kinsey, C. DeVault, A. Boltasseva, V. M. Shalaev, Near-zero-index materials for photonics. *Nat. Rev. Mater.* **4**, 742–760 (2019).
55. E. R. Vesseur, T. Coenen, H. Caglayan, N. Engheta, A. Polman, Experimental verification of n=0 structures for visible light. *Phys. Rev. Lett.* **110**, 013902 (2013).

56. N. P. Jouppi, C. Young, N. Patil, D. Patterson, G. Agrawal, R. Bajwa, S. Bates, S. Bhatia, N. Boden, A. Borchers, R. Boyle, P.-l. Cantin, C. Chao, C. Clark, J. Coriell, M. Daley, M. Dau, J. Dean, B. Gelb, T. V. Ghaemmaghami, R. Gottipati, W. Gulland, R. Hagmann, C. R. Ho, D. Hogberg, J. Hu, R. Hundt, D. Hurt, J. Ibarz, A. Jaffey, A. Jaworski, A. Kaplan, H. Khaitan, A. Koch, N. Kumar, S. Lacy, J. Laudon, J. Law, D. Le, C. Leary, Z. Liu, K. Lucke, A. Lundin, G. MacKean, A. Maggiore, M. Mahony, K. Miller, R. Nagarajan, R. Narayanaswami, R. Ni, K. Nix, T. Norrie, M. Omernick, N. Penukonda, A. Phelps, J. Ross, M. Ross, A. Salek, E. Samadiani, C. Severn, G. Sizikov, M. Snelham, J. Souter, D. Steinberg, A. Swing, M. Tan, G. Thorson, B. Tian, H. Toma, E. Tuttle, V. Vasudevan, R. Walter, W. Wang, E. Wilcox, D. H. Yoon, *In-Datacenter Performance Analysis of a Tensor Processing Unit. Proc. ISCA '17* (2017).
57. Nvidia. Inference Platforms for HPC Data Centers | NVIDIA Deep Learning AI; https://www.nvidia.cn/deep-learning-ai/inference-platform/hpc/.
58. Y. Cassivi, L. Perregrini, P. Arcioni, M. Bressan, K. Wu, G. Conciauro, Dispersion characteristics of substrate integrated rectangular waveguide. *IEEE Microw. Wirel. Compon. Lett.* **12**, 333–335 (2002).
59. Y. Zhou, H. Zheng, I. I. Kravchenko, J. Valentine, Flat optics for image differentiation. *Nat. Photonics* **14**, 316–323 (2020).
60. Online Horse Video; http://3g.163.com/v/video/VXI1LO67N.html.

Acknowledgments

Funding: Y.L. acknowledges partial support from the National Natural Science Foundation of China (NSFC) under grants 62022045 and 62071272. **Author contributions:** Y.L. conceived the idea and supervised the project with J.W. and Q.D. H.L. carried out the analytical derivations and full-wave simulations and partially launched the experiments. P.F. designed the image processing system and completed the experiments. Z.Z. and W.S. assisted in assembling the tested prototypes and constructed the experiment setup. All authors discussed the theoretical and numerical aspects, interpreted the results, and contributed to the preparation and writing of the manuscript. **Competing interests:** The authors declare that they have no competing interests. **Data and materials availability:** All data needed to evaluate the conclusions in the paper are present in the paper and/or the Supplementary Materials. Additional data and codes related to this paper have been deposited in Zenodo repository and may be available at https://doi.org/10.5281/zenodo.6635986.

Submitted 20 April 2022
Accepted 13 June 2022
Published 27 July 2022
10.1126/sciadv.abq6198

ScienceAdvances

Performing calculus with epsilon-near-zero metamaterials

Hao LiPengyu FuZiheng ZhouWangyu SunYue LiJiamin WuQionghai Dai

Sci. Adv., 8 (30), eabq6198. • DOI: 10.1126/sciadv.abq6198

Science Advances (ISSN) is published by the American Association for the Advancement of Science. 1200 New York Avenue NW, Washington, DC 20005. The title *Science Advances* is a registered trademark of AAAS.